

Cite this: *Analyst*, 2012, **137**, 2933

www.rsc.org/analyst

PAPER

Transport of redox probes through single pores measured by scanning electrochemical-scanning ion conductance microscopy (SECM-SICM)^{†‡}

Celeste A. Morris, Chiao-Chen Chen and Lane A. Baker*

Received 30th November 2011, Accepted 16th January 2012

DOI: 10.1039/c2an16178h

We report scanning electrochemical microscopy-scanning ion conductance microscopy (SECM-SICM) experiments that describe transport of redox active molecules which emanate from single pores of a track-etch membrane. Experiments are performed with electrodes which consist of a thin gold layer deposited on one side of a nanopipet. Subsequent insulation of the electrode with parylene results in a hybrid electrode for SECM-SICM measurements. Electrode fabrication is straightforward and highly parallel. For image collection, ionic current measured at the nanopipet both controls the position of the electrode with respect to the membrane surface and reports the local conductance in the vicinity of the nanopipet, while faradaic current measured at the Au electrode reports the presence of redox-active molecules. Application of a transmembrane potential difference affords additional control over migration of charged species across the membrane.

Introduction

Scanning ion-conductance microscopy (SICM) is a multi-purpose scanned probe technique with unique advantages in physiological settings.^{1–3} Non-contact image collection,⁴ robust feedback, multiple image collection modes^{1,2,5–10} and high resolution^{9,11} can be achieved with SICM. Applications of SICM include studies of surface topography of synthetic and biological membranes,^{2,12} measurement of ion transport through porous materials and ion channels,^{13–16} and observations of dynamic properties of live cells.^{7,17–19} Additionally, the combination of SICM with other microscopy techniques, such as scanning near-field optical microscopy,^{8,20–22} atomic force microscopy^{23,24} and confocal fluorescence microscopy,^{25–27} has resulted in hybrid techniques, which can supplement information measured. In this report, hybrid SECM-SICM has been performed with parylene C insulated Au nanopipet-electrodes to study diffusion and migration of positive ($\text{Ru}(\text{NH}_3)_6^{3+}$) and negative ($\text{Fe}(\text{CN})_6^{3-}$) redox probes through a porous polyimide membrane. With this technique, both ionic and faradaic current images of ions that permeate a single pore can be recorded.

Ionic current measured with SICM depends on both the resistance of the nanopipet-electrode and the resistance that develops when the nanopipet is in proximity to a surface, termed

the access resistance. As the pipet is advanced toward a sample surface, changes in the access resistance result in a distance-dependent current which serves as feedback for control of pipet position. The nanopipet is then raster-scanned over the surface in the x and y dimensions. Movements of the scanned probe and the total ion current, recorded simultaneously, can be monitored to generate two-dimensional maps of topography and ion current.

A drawback to SICM is an inherent lack of chemical specificity. Scanning electrochemical microscopy (SECM), known as the chemical microscope, is advantageous in this respect.^{28–31} Here, an ultramicroelectrode (UME), utilized as the scanned probe, reports spatially resolved electrochemical information. Numerous reports demonstrate the ability of SECM to measure molecular transport through synthetic and biological porous membranes.^{32–36} Through these experiments, quantification of the effects of diffusion, migration and convection to the overall flux of the system have been demonstrated.^{33–35,37,38} SECM, however, often suffers from poor resolution in comparison to SICM, largely due to difficulty in fabrication of electrodes with proper geometry. The development of hybrid SECM-SICM techniques offers an opportunity to control pipet position through SICM, and to measure faradaic electrochemical processes by SECM. Central to the development of SECM-SICM is electrode fabrication. Bard and coworkers reported an electrode design that involved a micropipet coated with a gold conductive layer, followed by an insulation layer of electrophoretic paint.³⁹ In the first demonstration of functional SECM-SICM, a similar approach to electrode fabrication was described by Hersam and co-workers.⁴⁰ In this study, atomic layer deposition of aluminum oxide was performed to insulate a gold-coated nanopipet followed by focused ion beam (FIB) milling to

Department of Chemistry, Indiana University, 800 E. Kirkwood Avenue, Bloomington, Indiana, 47405. E-mail: lanbaker@indiana.edu; Fax: + (812) 856-8300; Tel: + (812) 856-1873

[†] This article is part of a themed issue highlighting the targeted study of single units, such as molecules, cells, organelles and pores – The “Single” Issue, guest edited by Henry White.

[‡] Electronic supplementary information (ESI) available. See DOI: 10.1039/c2an16178h

expose the nanopipet pore and electrode surface. More recently, Matsue and co-workers insulated a Au sputtered nanopipet with electrophoretic paint.⁴¹ FIB milling exposed a ring-disk electrode around the nanopipet opening. A different approach to fabrication of carbon electrodes makes use of a theta pipet and was demonstrated recently by Korchev and coworkers.⁴² One barrel of the theta pipet was filled with electrolyte and used for SICM feedback. A carbon electrode was fabricated in the second barrel through pyrolysis of butane in an inert atmosphere.

Here, we demonstrate simple, bulk fabrication of SECM-SICM electrodes by parylene C insulation of Au-coated nanopipets. Parylene C can insulate high-aspect features at the same rate as low-aspect regions through vapor deposition and is a good candidate to provide a uniform, pin-hole free insulation layer.^{43–47} Additionally, a single run can coat multiple nanopipets to produce numerous SECM-SICM electrodes with similar exposed areas. Applications of these electrodes to measurement of redox probes that diffuse through nanopore membranes are demonstrated.

Experimental

Materials

Ruthenium hexammine trichloride, potassium ferricyanide (STREM Chemicals, Newburyport, MA) and potassium chloride (Mallinckrodt, Philipsburg, NJ) all >99% purity were used as received. Solutions were prepared with 18.2 MΩ·cm Milli-Q water and pH was adjusted to 7.4. Potassium iodide (Mallinckrodt, Philipsburg, NJ), and sodium hypochlorite (13% active chlorine, Acros, Morris Plains, NJ) were used to etch nanoporous membranes. Dichloro-[2,2]-paracyclophane (parylene C dimer, SCS Coatings, Indianapolis, IN) was used as received for electrode insulation. Poly-(dimethylsiloxane) (Sylgard 184, Dow Corning, Midland, MI) was used to mask the tips of nanopipets in the microelectrode insulation process.

Electrode fabrication and characterization

Quartz capillaries (Sutter Instruments, Novato, CA) with 1.0 mm outer diameter and 0.7 mm inner diameter were pulled with a P-2000 CO₂-laser pipet puller (Sutter Instruments, Novato, CA) to form two, symmetric nanopipets with program H = 640, F = 3, V = 41, D = 195, P = 185. This produces nanopipets with inner diameters of 200–230 nm ($n = 20$) as observed from scanning electron microscopy.

Thermal deposition (Auto 306, Edwards) of a Cr adhesion layer (12 nm at 2 Å s⁻¹) followed by a Au layer (188 nm at 2 Å s⁻¹) was used to create the SECM electrode on one half of a nanopipet (Fig. 1a). Insulation of nanopipet-electrodes was performed by parylene C deposition (Labcoater 2/PDS 2010, SCS coatings) where nanopipet-electrodes were first stood on end in a thin polydimethylsiloxane (PDMS) layer and vapor deposition of parylene C was performed. After insulation, a micromanipulator was used to raise the pipets directly out of the PDMS mask which left the entire electrode insulated by parylene C except for the masked region at the tip. Up to 40 electrodes were fabricated in this fashion in a single run. A success rate of >50% for nanopipets with tips less than 500 nm outer diameter and

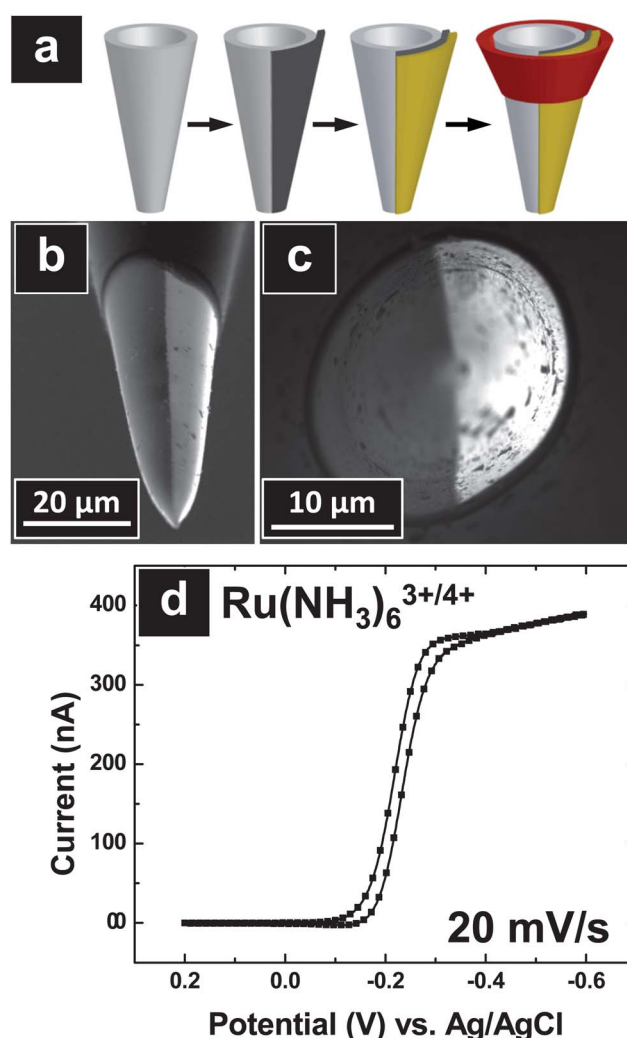


Fig. 1 (a) Schematic of electrode fabrication. From left to right: bare quartz nanopipet, nanopipet with 12 nm Cr adhesive layer, addition of 188 nm Au, and finally parylene C insulated pipet-electrode. (b) Scanning electron micrograph of nanopipet-electrode with an exposed electrode area of $3.8 \times 10^3 \mu\text{m}^2$ and a clear distinction between the Au electrode (right), quartz (left) and parylene C insulation (top). (c) The tip region of the electrode which demonstrates the quartz on the left and Au on the right with a tip diameter of 310 nm and a cone angle of 18.5°. (d) Electrochemical response of the electrode from (b) and (c) in 10 mM $\text{Ru}(\text{NH}_3)_6\text{Cl}_3/100 \text{ mM KCl}$ at a scan rate of 20 mV s⁻¹.

exposed Au electrodes of length $100 \pm 20 \mu\text{m}$ ($n = 20$) was achieved.

After fabrication, all electrodes were characterized by scanning electron microscopy (FE-SEM, FEI Quanta-FEG) and cyclic voltammetry (CHI660 potentiostat, CH Instruments, Austin, TX), Fig. 1b–d. The scanning electron micrograph in Fig. 1b displays the gold layer on the right side of the pipet, quartz on the left and parylene C insulation at the top. The electrode area is $\sim 3.8 \times 10^3 \mu\text{m}^2$, and resulted in a quasi steady-state current of 380 nA in solution which contained 10 mM $\text{Ru}(\text{NH}_3)_6\text{Cl}_3/100 \text{ mM KCl}$ as supporting electrolyte. The steady-state electrochemical response of this electrode in 10 mM $\text{K}_3\text{Fe}(\text{CN})_6/100 \text{ mM KCl}$ was 230 nA, SI Figure 1c.

Membrane preparation and characterization

Nanoporous polyimide membranes were prepared through the track-etch process as described previously.¹² Briefly, a polyimide film, irradiated with heavy ions, was subsequently chemically-etched to create a porous membrane. Here, membranes (polyimide, track density 10^4 tracks/cm², thickness 25 μm , it4ip, Belgium) were immersed in 13% sodium hypochlorite solution at 70 °C to develop cylindrical nanopores. After exposure to etchant, membranes were placed in 1M potassium iodide solution for 30 min to neutralize the etch process. Pore diameters were further characterized with scanning electron microscopy (SEM) to produce well-characterized standards for examination with SECM-SICM. Statistical analysis of pore sizes was performed with ImageJ (National Institutes of Health, MD).

Instrumentation

SICM experiments were performed with a ScanIC scanning ion conductance microscope (ionscope, Ltd, London, UK) in conjunction with an Axopatch 200B current amplifier (Molecular Devices, Union City, CA). To perform SECM-SICM with migration studies, a five electrode system was utilized, adapted from a previously established four-electrode ion-conductance microscope, Fig. 2a. Here, the pipet electrode (PE) consists of a Ag/AgCl wire back-inserted into the nanopipet-electrode, which was filled with 0.1M KCl. For all of the experiments reported in this study, PE was biased at +100 mV referenced to the Ag/AgCl reference electrode (RE), which was also in the top chamber. A Pt counter electrode (CE) and the Ag/AgCl reference electrode (RE) were connected to a counter electrode driver (CE driver) and both were located in the top chamber. To apply a transmembrane potential difference across the membrane, a Ag/AgCl working electrode (WE) was mounted in the bottom chamber of the diffusion cell. Finally, the gold electrode (AuE) was referenced to the RE through the counter electrode driver. Faradaic current was collected at the AuE, Fig. 2b, while ion current was collected at the PE. No electrochemical response was obtained from Au under the parylene C layer. Under distance-modulated feedback, the electrode was modulated ~ 100 nm vertically at 800 Hz. The horizontal and vertical positions of the nanopipet and the magnitude of dc ion current were measured to produce topographic and dc current images, respectively. Simultaneously, SECM images were collected *via* the auxiliary channel of SICM. All images were analyzed with SICM Image Viewer (ionscope Ltd., London, UK) and Gwyddion (David Nečas and Petr Klapetek, Brno, Czech Republic).

Collection of images at membranes

With the electrodes described in Fig. 1 and the experimental configuration shown in Fig. 2, transport through porous membranes was examined. Membranes with nominal pore diameter of 900 nm were masked in clear tape with a 1-mm-diameter through-hole which exposed the porous membrane to electrolyte solutions on both sides, Fig. 2a. Membranes were further masked with water-resistant epoxy, as described previously,¹³ such that only 4 pores were exposed to solution. Initially, both the upper and lower chambers were filled with 100 mM KCl as supporting electrolyte. To study the diffusion and migration of

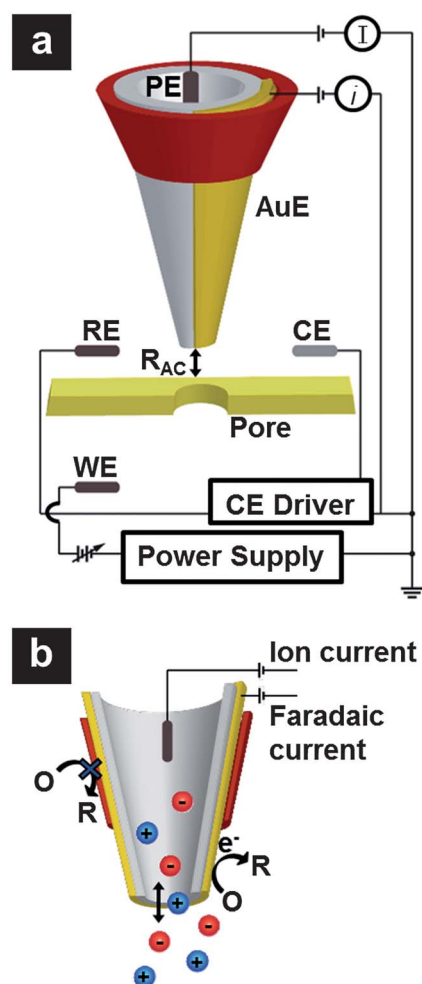


Fig. 2 (a) Schematic of a nanopipet-electrode for SECM-SICM measurements. A Ag/AgCl electrode, inside the nanopipet, serves as the pipet electrode (PE). The Au coating (AuE) is used to obtain faradaic current from reduction or oxidation of redox probe molecules which permeate a porous membrane. A Ag/AgCl electrode in the top chamber serves as the reference electrode (RE), while a Ag/AgCl electrode in the bottom chamber serves as the working electrode (WE) to apply a transmembrane potential difference *via* the power supply. A Pt counter electrode (CE) is controlled by the counter electrode driver (CE driver). (b) Close-up of the nanopipet-electrode where ions traverse the narrow pipet opening. Redox ions are oxidized/reduced only at the exposed surface of the AuE (right, golden) but not at the parylene C insulated region (left, red).

redox probes, the bottom chamber of the diffusion cell was filled with solutions of varied concentrations of redox probes (*e.g.* 25 or 100 mM $\text{K}_3\text{Fe}(\text{CN})_6$ with 100 mM KCl, or 10 mM $\text{Ru}(\text{NH}_3)_6\text{Cl}_3$ with 100 mM KCl).

Results and discussion

SECM-SICM

Distance-modulated image collection was performed to obtain topography, ion current (conductance) and faradaic current images of single pores on the membrane. Topography of a 900-nm-diameter pore, Fig. 3a, was imaged with the electrode at an electrode-surface distance of 120 nm. From the SICM image,

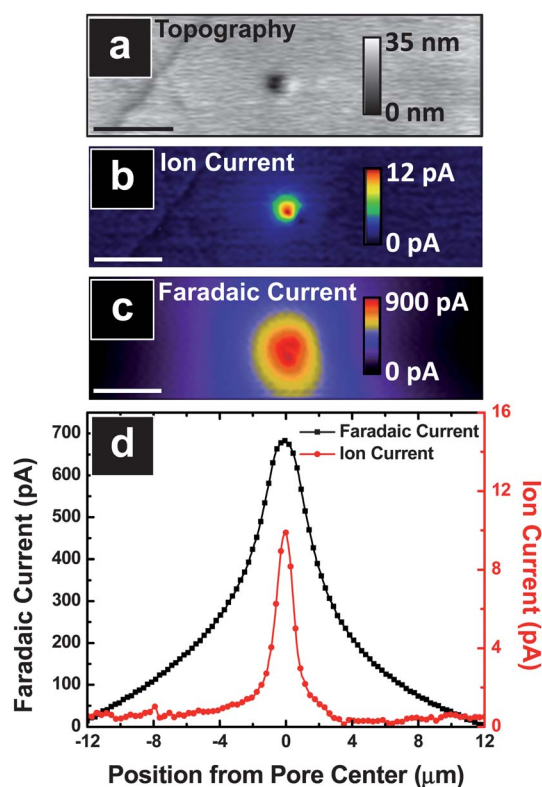


Fig. 3 (a) Topography imaged with the nanopipet-electrode of a 900 nm pore in the polyimide membrane. (b) Ion current and (c) faradaic current of Fe(CN)₆^{3-/4-} reduction recorded with the AuE as the pore was imaged. All images were recorded simultaneously with a transmembrane potential of -300 mV vs. Ag/AgCl and a probe-surface distance of 120 nm. Scale bar in all images is 2.0 μm. (d) Cross sections of ion current and faradaic current images b and c (note scale difference).

a pore diameter of 1.0 ± 0.1 μm ($n = 5$) was measured, which overestimates the pore size as measured by SEM, in agreement with previous reports.¹² Conductance images were recorded at the same time by the measurement of the dc component of the ion current signal. For data shown in Fig. 3, the top chamber of the diffusion cell housed an aqueous solution of 100 mM KCl and the bottom chamber housed 100 mM K₃Fe(CN)₆/100 mM KCl. To enhance ion migration between two chambers, the working electrode in the bottom chamber of the diffusion cell was biased at a constant transmembrane potential difference of -300 mV (vs. the Ag/AgCl reference electrode in the top chamber). Transport of ions and the subsequent increase of solution conductivity in the vicinity of the pore resulted in an increase of the ion current signal, Fig. 3b. Under the same conditions, faradaic current was measured simultaneously, as shown in Fig. 3c. Here, the AuE was biased at -100 mV (vs. Ag/AgCl reference electrode), a potential sufficient to reduce Fe(CN)₆³⁻ in the vicinity of the electrode (SI Figure 1c). The working electrode (present in the bottom half of the diffusion cell) drives not only K⁺ and Cl⁻ ions, but also charged electrochemical species, such as Fe(CN)₆³⁻. Here, faradaic current measured in the vicinity of the pore is greater than at regions away from the pore.

Due to the high resistance of the PE (~ 100 MΩ, a result of the relatively small pipet opening ~ 200 nm), conductance variations

around the pore are observed as differences in the total ion current on the order of 10 pA. Total ion currents measured by the nanopipet were on the order of 1 nA under conditions here. In comparison, due to the larger electrode size (\sim micrometres) of the AuE, a much greater faradaic response (900 pA) is recorded. In addition to the larger electrode size, the fact that a significant fraction of the total surface area of the AuE is located 50–150 nanometres from the nanopipet opening results in lower resolution, compared to the true pore dimension. Resolution of electrochemical image collection recorded with the AuE employed here might also suffer if electrochemical species were present at significant concentrations in the top half of the diffusion cell, which would result in a large background current. For studies reported here, the AuE geometry and size perform adequately for measurement of electrochemical species, as the initial concentration of redox probes in the top half of the diffusion cell is essentially zero, which results in little to no background current in regions away from the pore opening. This redox probe-dependent difference in resolution is shown in Fig. 3d, where cross sections of the current response over the single pore are plotted. A Lorentzian fit of the faradaic current response gave a full width of half maximum (FWHM) of 5.7 μm, while the ion current gave 1.2 μm, both with high (0.98) correlation coefficient. This difference in resolution is dependent on the nanopipet-electrode geometry employed here and does not reflect an inherent difference in resolution of SECM vs. SICM.

The influence of a transmembrane potential on both the ion current and faradaic current was examined in more detail. For these experiments, initially no KCl concentration gradient was used (100 mM KCl was placed both in the top and the bottom chamber of the diffusion cell) while the pore was imaged at a constant electrode-surface distance of 120 nm. Further, for initial measurements, no redox probe was present. Consecutive images of a single pore were recorded at 0, -100 , -300 and -500 mV vs. Ag/AgCl transmembrane potential. The maximum peak currents observed over the single pore for both ion current and faradaic current are shown in Fig. 4a and b. Under these conditions, a linear change in ion current (conductance) with applied transmembrane potential measured at the PE is clearly obvious, Fig. 4a, ▲. As no redox probe is initially present, no change in the faradaic current signal is detected at the AuE (-100 mV vs. Ag/AgCl), Fig. 4b, △. Redox probe was then added to the bottom chamber of the diffusion cell to a final concentration of 25 mM ferricyanide. Peak currents measured over a single pore for this condition report an increase in both current responses, ionic and faradaic, as the total ion concentration (and conductivity) in the vicinity of the pore is increased for the ion current measured, Fig. 4a, ●. The redox probe concentration is also increased as reported by the AuE, Fig. 4b, ○. Increase of the redox probe concentration in the bottom chamber to 100 mM K₃Fe(CN)₆/100 mM KCl, resulted in similar increases in each current signal (ion current: Fig. 4a, ■; faradaic current: Fig. 4b, □), which further demonstrates the interdependence but uniqueness of each signal recorded.

Chemical imaging: effects of redox probe identity

The experiments described in Fig. 3 and 4 demonstrate the ion current measured in SICM indeed responds to changes in

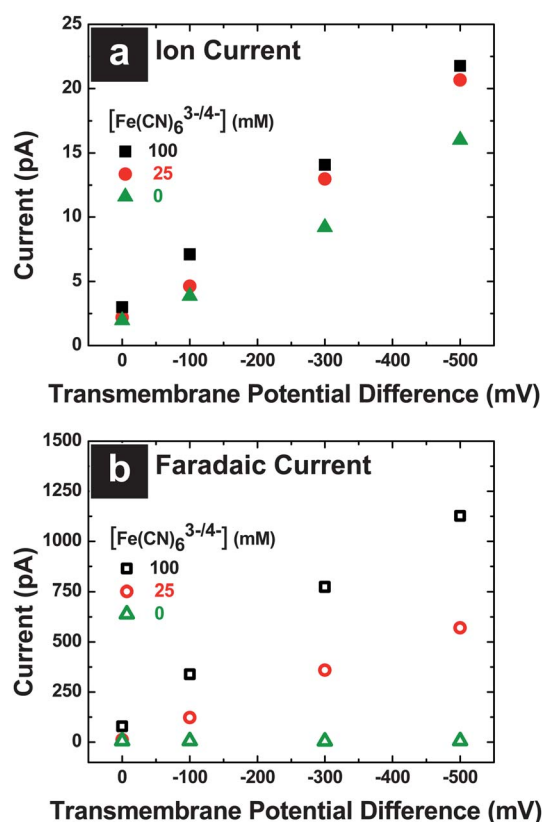


Fig. 4 (a) Ion current measured with the pipet electrode biased at +100 mV vs. Ag/AgCl in the absence (\blacktriangle) and the presence of 25 mM (\bullet) and 100 mM (\blacksquare) K₃Fe(CN)₆ in the bottom chamber. (b) Faradaic current measured with the AuE biased at -100 mV vs. Ag/AgCl in the absence (\triangle) and the presence of 25 mM (\circ) and 100 mM (\square) K₃Fe(CN)₆ in the bottom chamber.

solution conductivity, which occur upon the addition of a redox probe. SECM affords an opportunity to examine chemical identities based on the electrochemical oxidation-reduction potential of a redox probe. To examine this in detail, two redox probes, ferricyanide and ruthenium hexamine were chosen. Ferricyanide is an anionic redox probe which is reduced to ferriyanide at moderate negative potentials (≤ -100 mV vs. Ag/AgCl). In contrast, ruthenium hexamine is a cationic redox probe which is oxidized at moderate negative potentials (≤ -400 mV

vs. Ag/AgCl). Here, one redox probe was added to the bottom of the diffusion cell and a transmembrane potential was applied across the membrane. As configured, under a negative transmembrane potential (*i.e.* WE biased at a negative potential vs. Ag/AgCl), anions are driven to the top chamber of the diffusion cell, whereas cations are driven to the bottom chamber. When the polarity of the transmembrane potential is reversed, the direction of driven ion transport is also reversed. Peak currents over a single pore were measured at the AuE for each redox probe, as shown in Fig. 5.

In the first case, with 100 mM Fe(CN)₆^{3-/4-}/100 mM KCl in the bottom chamber, faradaic current was detected at the AuE (biased at -100 mV vs. Ag/AgCl) due to Fe(CN)₆^{3-/4-} reduction when a negative transmembrane potential was applied. At more negative transmembrane potentials, a greater driving force for anion transport is present, and thus results in higher faradaic currents as observed in Fig. 5. In the case of ferricyanide, for positive transmembrane potentials, little to no faradaic current is recorded.

In the second case, with 10 mM Ru(NH₃)₆^{3+/4+}/100 mM KCl in the bottom chamber, the opposite transport directionality was observed. Faradaic current was detected at the AuE (biased at -400 mV vs. Ag/AgCl) due to Ru(NH₃)₆^{3+/4+} oxidation when positive transmembrane potentials were applied. However, no faradaic response is observed when a negative transmembrane potential was utilized.

The spatial distributions of the faradaic response as a function of applied transmembrane potentials are shown in Fig. 5 (b–e). This demonstrates that electrochemical detection for redox probes of opposite charge can be turned “on” and “off”, which further highlights the chemical nature of the measurements recorded with SECM.

Conclusions

We have demonstrated that thermally evaporated Au electrodes, insulated with parylene C on nanopipets can serve as an SECM-SICM electrode. The advantages of this electrode include a fast and simple bulk-fabrication method and high-resolution capabilities. In addition to faithful measurement of surface topography, these electrodes can detect diffusion and migration of positively and negatively charged redox probes which permeate a nanoporous membrane. Importantly, SECM-SICM benefits from the ability to control the position of the electrode with high

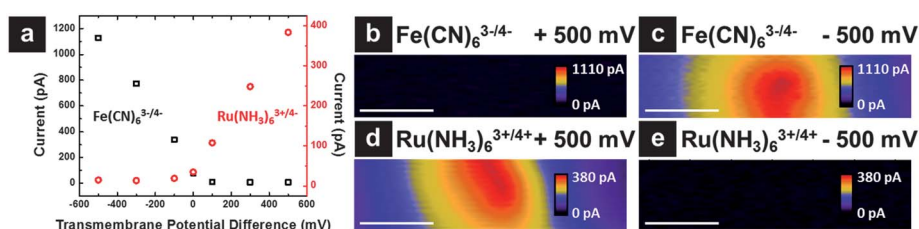


Fig. 5 (a) Faradaic current of Fe(CN)₆³⁻ reduction (100 mM K₃Fe(CN)₆/100 mM KCl bottom chamber) and Ru(NH₃)₆³⁺ oxidation (10 mM Ru(NH₃)₆Cl₃/100 mM KCl bottom chamber) at various transmembrane potential differences. (b) Fe(CN)₆³⁻ does not migrate to the top chamber of the diffusion cell with a transmembrane potential difference of +500 mV vs. Ag/AgCl, however, migration of Fe(CN)₆³⁻ readily occurs with a transmembrane potential difference of -500 mV vs. Ag/AgCl. (c). (d) Ru(NH₃)₆³⁺ oxidation occurs with a transmembrane potential difference of +500 mV due to enhanced migration but is not observed at -500 mV vs. Ag/AgCl. (e). AuE biased at -100 mV vs. Ag/AgCl for Fe(CN)₆³⁻ reduction and -400 mV vs. Ag/AgCl for Ru(NH₃)₆³⁺ oxidation. Scale bar is 2.0 μm for all images.

precision through SICM feedback, but still retains chemical information afforded from oxidation/reduction reactions measured with the SECM electrode.

Acknowledgements

The support of the American Heart Association, Research Corporation and National Institutes of Health are gratefully acknowledged. John Poehlman and Andy Alexander of Electronic Instrument Services, Indiana University, Department of Chemistry are thanked for building the counter electrode driver. The collaboration of Kirstin C. Morton, Rahul Thakar and Maksymilian Derylo for parylene C insulation steps, Yi Zhou for track-etched membranes and Niya Sa for pipet programs is sincerely appreciated.

References

- 1 P. K. Hansma, B. Drake, O. Marti, S. A. Gould and C. B. Prater, *Science*, 1989, **243**, 641–643.
- 2 Y. E. Korchev, C. L. Bashford, M. Milovanovic, I. Vodyanoy and M. J. Lab, *Biophys. J.*, 1997, **73**, 653–658.
- 3 C. B. Prater, P. K. Hansma, M. Tortonesi and C. F. Quate, *Rev. Sci. Instrum.*, 1991, **62**, 2634–2638.
- 4 J. Gorelik, N. N. Ali, S. H. Sheikh Abdul Kadir, M. Lab, P. Stojkovic, L. Armstrong, E. V. Sviderskaya, Y. A. Negulyaev, D. Klenerman, D. C. Bennett, M. Lako, S. E. Harding, M. Stojkovic and Y. E. Korchev, *Tissue Eng., Part C*, 2008, **14**, 311–318.
- 5 S. A. Mann, G. Hoffmann, A. Hengstenberg, W. Schuhmann and I. D. Dietzel, *J. Neurosci. Methods*, 2002, **116**, 113–117.
- 6 R. Proksch, R. Lal, P. K. Hansma, D. Morse and G. Stucky, *Biophys. J.*, 1996, **71**, 2155–2157.
- 7 A. I. Shevchuk, J. Gorelik, S. E. Harding, M. J. Lab, D. Klenerman and Y. E. Korchev, *Biophys. J.*, 2001, **81**, 1759–1764.
- 8 M. Bocker, B. Anczykowski, J. Wegener and T. Schaffer, *Nanotechnology*, 2007, **18**, 145505.
- 9 P. Novak, C. Li, A. I. Shevchuk, R. Stepanyan, M. Caldwell, S. Hughes, T. G. Smart, J. Gorelik, V. P. Ostanin, M. J. Lab, G. W. J. Moss, G. I. Frolenkov, D. Klenerman and Y. E. Korchev, *Nat. Methods*, 2009, **6**, 279–281.
- 10 Y. Takahashi, Y. Murakami, K. Nagamine, H. Shiku, S. Aoyagi, T. Yasukawa, M. Kanzaki and T. Matsue, *Phys. Chem. Chem. Phys.*, 2010, **12**, 10012–10017.
- 11 A. I. Shevchuk, G. I. Frolenkov, D. Sánchez, P. S. James, N. Freedman, M. J. Lab, R. Jones, D. Klenerman and Y. E. Korchev, *Angew. Chem., Int. Ed.*, 2006, **45**, 2212–2216.
- 12 C.-C. Chen, M. A. Derylo and L. A. Baker, *Anal. Chem.*, 2009, **81**, 4742–4751.
- 13 C.-C. Chen, Y. Zhou and L. A. Baker, *ACS Nano*, 2011, 8404–8411.
- 14 Y. E. Korchev, Y. A. Negulyaev, C. R. W. Edwards, I. Vodyanoy and M. J. Lab, *Nat. Cell Biol.*, 2000, **2**, 616–619.
- 15 M. Böcker, S. Muschter, E. K. Schmitt, C. Steinem and T. E. Schäffer, *Langmuir*, 2009, **25**, 3022–3028.
- 16 C.-C. Chen and L. A. Baker, *Analyst*, 2011, **136**, 90–97.
- 17 A. Darszon, C. D. Wood, C. Beltrán, D. Sánchez, E. Rodríguez, J. Gorelik, Y. E. Korchev and T. Nishigaki, in *Methods Cell Biol.*, ed. G. A. W. Charles A. Ettensohn and M. W. Gary, Academic Press, 2004, vol. 74, pp. 545–576.
- 18 J. Gorelik, A. I. Shevchuk, G. I. Frolenkov, I. A. Diakonov, M. J. Lab, C. J. Kros, G. P. Richardson, I. Vodyanoy, C. R. W. Edwards, D. Klenerman and Y. E. Korchev, *Proc. Natl. Acad. Sci. U. S. A.*, 2003, **100**, 5819–5822.
- 19 M. Pellegrino, P. Orsini and F. De Gregorio, *Neurosci. Res.*, 2009, **64**, 290–296.
- 20 S. Shalom, K. Lieberman, A. Lewis and S. R. Cohen, *Rev. Sci. Instrum.*, 1992, **63**, 4061–4065.
- 21 Y. E. Korchev, M. Raval, M. J. Lab, J. Gorelik, C. R. W. Edwards, T. Rayment and D. Klenerman, *Biophys. J.*, 2000, **78**, 2675–2679.
- 22 A. Mannelquist, H. Iwamoto, G. Szabo and Z. Shao, *Appl. Phys. Lett.*, 2001, **78**, 2076–2078.
- 23 K. Lieberman, A. Lewis, G. Fish, S. Shalom, T. M. Jovin, A. Schaper and S. R. Cohen, *Appl. Phys. Lett.*, 1994, **65**, 648–650.
- 24 H. Taha, R. S. Marks, L. A. Gheber, I. Rouso, J. Newman, C. Sukenik and A. Lewis, *Appl. Phys. Lett.*, 2003, **83**, 1041–1043.
- 25 J. Gorelik, A. Shevchuk, M. Ramalho, M. Elliott, C. Lei, C. F. Higgins, M. J. Lab, D. Klenerman, N. Krauzewicz and Y. Korchev, *Proc. Natl. Acad. Sci. U. S. A.*, 2002, **99**, 16018–16023.
- 26 A. Shevchuk, P. Hobson, M. Lab, D. Klenerman, N. Krauzewicz and Y. Korchev, *Pflugers Arch.*, 2008, **456**, 227–235.
- 27 A. I. Shevchuk, P. Hobson, M. J. Lab, D. Klenerman, N. Krauzewicz and Y. E. Korchev, *Biophys. J.*, 2008, **94**, 4089–4094.
- 28 A. J. Bard, F. R. F. Fan, J. Kwak and O. Lev, *Anal. Chem.*, 1989, **61**, 132–138.
- 29 A. J. Bard, F.-R. F. Fan, D. T. Pierce, P. R. Unwin, D. O. Wipf and F. Zhou, *Science*, 1991, **254**, 68–74.
- 30 A. Schulte, M. Nebel and W. Schuhmann, *Annu. Rev. Anal. Chem.*, 2010, **3**, 299–318.
- 31 S. Amemiya, A. J. Bard, F.-R. F. Fan, M. V. Mirkin and P. R. Unwin, *Annu. Rev. Anal. Chem.*, 2008, **1**, 95–131.
- 32 E. R. Scott, H. S. White and J. B. Phipps, *Anal. Chem.*, 1993, **65**, 1537–1545.
- 33 B. D. Bath, R. D. Lee, H. S. White and E. R. Scott, *Anal. Chem.*, 1998, **70**, 1047–1058.
- 34 B. D. Bath, H. S. White and E. R. Scott, *Anal. Chem.*, 2000, **72**, 433–442.
- 35 B. D. Bath, E. R. Scott, J. B. Phipps and H. S. White, *J. Pharm. Sci.*, 2000, **89**, 1537–1549.
- 36 B. D. Bath, H. S. White and E. R. Scott, *Pharm. Res.*, 2000, **17**, 471–475.
- 37 E. R. Scott, A. I. Laplaza, H. S. White and J. B. Phipps, *Pharm. Res.*, 1993, **10**, 1699–1709.
- 38 E. R. Scott, J. B. Phipps and H. S. White, *J. Invest. Dermatol.*, 1995, **104**, 142–145.
- 39 D. A. Walsh, J. L. Fernández, J. Mauzeroll and A. J. Bard, *Anal. Chem.*, 2005, **77**, 5182–5188.
- 40 D. J. Comstock, J. W. Elam, M. J. Pellin and M. C. Hersam, *Anal. Chem.*, 2010, **82**, 1270–1276.
- 41 Y. Takahashi, A. I. Shevchuk, P. Novak, Y. Murakami, H. Shiku, Y. E. Korchev and T. Matsue, *J. Am. Chem. Soc.*, 2010, **132**, 10118–10126.
- 42 Y. Takahashi, A. I. Shevchuk, P. Novak, Y. Zhang, N. Ebejer, J. V. Macpherson, P. R. Unwin, A. J. Pollard, D. Roy, C. A. Clifford, H. Shiku, T. Matsue, D. Klenerman and Y. E. Korchev, *Angew. Chem., Int. Ed.*, 2011, **50**, 9638–9642.
- 43 M. A. Spivack, *Rev. Sci. Instrum.*, 1970, **41**, 1614.
- 44 K. C. Morton, C. A. Morris, M. A. Derylo, R. Thakar and L. A. Baker, *Anal. Chem.*, 2011, **83**, 5447–5452.
- 45 G. E. Loeb, M. J. Bak, M. Salcman and E. M. Schmidt, *IEEE Trans. Biomed. Eng.*, 1977, **24**, 121–128.
- 46 E. Artukovic, M. Kaempgen, D. S. Hecht, S. Roth and G. Gruner, *Nano Lett.*, 2005, **5**, 757–760.
- 47 M. A. Derylo, K. C. Morton and L. A. Baker, *Langmuir*, 2011, **27**, 13925–13930.